Check for updates

FSL-CP: a benchmark for small molecule activity few-shot prediction using cell microscopy images†

Son V. Ha, Lucas Leuschner and Paul Czodrowski [ID] *

Predicting small molecule activities using information from high-throughput microscopy images has been shown to tremendously increase hit rates and chemical diversity of the hits in previous drug discovery projects. However, due to high cost of acquiring data or ethical reasons, data sparsity remains a big challenge in drug discovery. This opens up the opportunity for few-shot prediction: fine-tuning a model on a low-data assay of interest after pretraining on other more populated assays. Previous efforts have been made to establish a benchmark for few-shot learning of molecules based on molecular structures. With cell images as a molecular representation, methods in the computer vision domain are also applicable for activity prediction. In this paper, we make two contributions: (a) a public data set for few-shot learning with cell microscopy images for the scientific community and (b) a range of baseline models encompassing different existing single-task, multi-task and meta-learning approaches.

1   Introduction

High-throughput imaging (HTI) has been a powerful tool in drug discovery, having yielded many biological discoveries.[1–3] It often involves capturing the morphological changes of cells induced by chemical compounds and quantifying these changes into a large set of numerical features[4] such as staining intensity, texture, shape and spatial correlations. They act as 'fingerprints' that can be used to characterise compounds in a relatively unbiased way. This technique, known as morphological profiling, has proven to be useful for a variety of applications, such as optimizing the diversity of compound libraries,[5] determining the mechanism of action of compounds,[6–8] and clustering genes based on their biological functions.[9,10]

Cell painting is a morphological profiling method in which cells are perturbed with a compound, have their different compartments stained using six dyes, and have their images of the five fluorescence channels captured.[4] Cell painting data have been used for a range of applications, from predicting mitochondrial toxicity,[3,11] *in vitro* toxicity,[12] hit identification,[13] and more. In addition, cell painting can be used in combination with other modalities to enhance prediction such as chemical structure[14] and gene expression data.[15]

1.1   Small molecule activity prediction

Prediction of small molecule activity against a drug target is an important task in drug discovery. It helps identify and optimise

JGU Mainz, Germany. E-mail: czodpaul@uni-mainz.de

compounds for a desired activity, as well as recognise and avoid off-target activities. This leads to the identification of compounds with the highest potential in the early drug discovery pipeline.

HTI data have been used in bioactivity prediction by Simm *et al.*[16] in two drug discovery projects, which led to a tremendous increase in hit rates by 50- to 250-fold, while increasing the chemical structure diversity of the hits. In these projects, only 1.6% of the label matrix is filled, for over 500 000 compounds and 1200 prediction tasks. This reflects the need for a modeling paradigm which can not only adapt to new tasks quickly with little data, but also leverage the availability of many low-data related tasks. We find that this setting is ideal to form a few-shot learning challenge.

1.2   Few-shot learning

In the few-shot learning setting, there is not one big dataset D to learn from, but instead many small datasets we called tasks, denoted T. The aim of few-shot methods is to generalise over new tasks $\{T_u\}_{u=1}^{U} \in D_{\text{test}}$ efficiently with only a small number of available datapoints. Each task T_u consists of a support set S for learning and a query set Q for evaluation, $T_u = \langle S, Q \rangle$. Typically the size of support set S is very small to reflect the low-data setting.

Few-shot models adapt efficiently to low-data tasks by using an advantage initialisation of their parameters, normally through some sort of pretraining on a large data corpus such as a set of auxiliary tasks $\{T_v\}_{v=1}^{V} \in D_{\text{train}}$. We expect that knowledge gained from pretraining can be transferred effectively to new unseen tasks, so that models can quickly learn these new tasks using only little data. This can be compared to, for example, a person who already has prior knowledge of music picking up a new musical instrument relativelyquickly with little demonstration.

Most state-of-the-art few-shot methods come from computer vision and natural language processing domains.[17–21] Drug discovery is another field where there is growing interest in few-shot learning,[22] since data scarcity is a common setting for many prediction tasks. In this paper, we propose to expand another challenge in drug discovery to the few-shot learning area: the aforementioned small molecule activity prediction with cell imaging data. We find that this is a real-world scientific problem with an ideal few-shot setting: there are many related low-data tasks convenient for knowledge transfer between each other. Furthermore, with cell images as a molecular representation, methods in the computer vision domain can be adapted for activity prediction. We believe that the field of cell imaging/analysis would greatly benefit from these algorithmic innovations.

In this paper, we make two contributions:

• A data set for few-shot prediction of small molecule activity using cell microscopy images, which we named FSL-CP. The dataset is curated so that it is easy for future researchers to experiment with their few-shot methods.

• A benchmark of models encompassing different existing single-task, multi-task and meta-learning approaches on the dataset. This acts as both a diverse baseline for future algorithms and a means to study the strengths and weaknesses of different modelling paradigms.

2 Methods

### 2.1 FSL-CP: few-shot learning data set with cell microscopy images

The FSL-CP dataset comprises compounds at the intersection of ChEMBL[23] version 31 and the cell painting[4] public dataset. We provide an overview of the data construction process below (Fig. 1), and the exact reproducible source code is available on GitHub, at **https://github.com/czodrowskilab/FSL_CP_DataPrep**.

Original cell painting data set. Cell microscopy images come from Bray *et al.*[4] and contain 919 265 five-channel views, representing 30 616 compounds. In this cell painting protocol, U2OS cells have 8 major organelles and sub-compartments stained using a mixture of 6 fluorescent dyes, resulting in 5 different image channels. A CellProfiler[24] pipeline is then used to extract 1783 single-cell morphological features from those images.

Labelling the compounds. For this project we focus on small molecule activity assays (*e.g.* IC_{50} and EC_{50}) available in the ChEMBL database. We query activity data for all the compounds in the original cell painting dataset using their InChiKey. We follow a similar data processing strategy to that by Hofmarcher *et al.*[25] For each assay, both the activity comments from the experimenter and the pChEMBL values (numerical value for activity on a negative logarithmic scale) are retrieved. Duplicate labels are resolved either by averaging if they are pChEMBL values, or by majority voting if they are activity comments. The pChEMBL values are restricted to only between 4 and 10, and the activity comments are also chosen to only be spelling variants of 'active' and 'inactive'. The final modeling task is defined as an assay after being binarized, either with a threshold on the pChEMBL value, or based on the activity comments. For the pChEMBL values specifically, we use three thresholds for each assay: 5.5, 6.5, and 7.5, which results in three separate modelling tasks. Lastly, we filter out to only allow tasks with at least 10 active and 10 inactive labelled compounds.

Processing the cell painting data. The images, as well as morphological features aggregated at well-level and metadata, can be found at the 'Cell Image Library'. The five dye channels
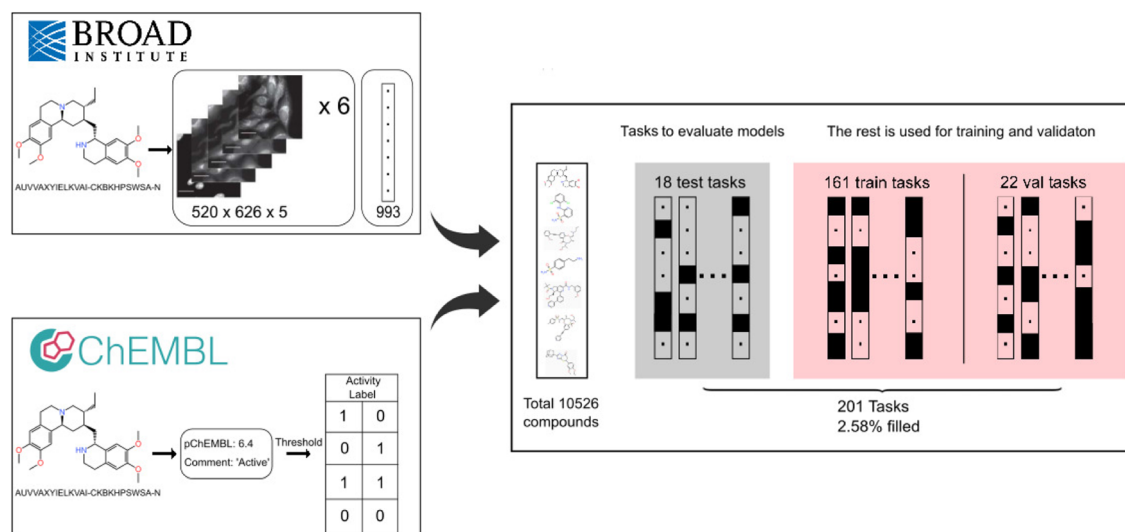
Fig. 1 FSL–CP data curation and processing. Cell painting images and features from CellProfiler[24] come from Bray *et al.*[4] Each well is represented by six 520 × 696 × 5 images and a feature vector of length 993. Small molecule activity labels are retrieved from assays in ChEMBL31.[23] Then a threshold procedure is applied to binarise the labels, producing different tasks from assays. The intersection of the two sources results in 10 526 unique compounds and 201 prediction tasks. 18 tasks are chosen for model evaluation based on a set of criteria, and the rest are for training and validation (referred to as auxiliary tasks).

are concatenated along the third dimension, converted into 8 bits, and have their 0.0028% outlier bits removed.[25] The images are further normalised prior to modelling. For the well-level morphological features, we remove columns that are highly correlated (correlation coefficient >0.95), or have only one value. Finally, we standardize features by removing the mean and scaling to unit variance.

Features. At the end, each data point of FSL-CP corresponds to one well, represented by six $520 \times 696 \times 5$ images (for six views in a well), and by a feature vector of length 993. We refer to them as CP images and CP features, respectively. SMILES strings and InChiKey are also provided, although for this study we only focus on the cell images and information which comes from them.

Deep learning embedding. We also create an 'enhanced' set of CP features by concatenating the original CP features with embeddings from ResNet50 (ref. 26) pretrained on ImageNet,[27] akin to the method used by Schiff *et al.*[28] This embedding provides the input vector with abstract high-level neural-network-based features. For each well, we run the six $520 \times 696 \times 5$ views through ResNet50 to generate six embeddings, which are then averaged to create one final embedding of length 1000. We tried different variants of ResNet and Inception:[29,30] ResNet18, ResNet50, ResNet101, ResNet152, inception_resnet_v2, and inception_v3. We ended up settling on ResNet50, which yields the best performance on our dataset despite being a simple model. It

should be noted that the length of the embedding can be further tuned to boost predictive performance.

Pretraining, validation and test splits. The models are evaluated on 18 tasks which we will call test set D_{test}. The other 183 tasks, referred to as auxiliary tasks, are used for model pretraining. They are randomly split into train set D_{train} and validation set D_{val}, consisting of 161 and 22 tasks, respectively. The test tasks are selected based on the following criteria:

● Tasks in D_{test} do not share the same targets as those in the D_{train} and D_{val}, unless a target is unknown (denoted as 'unchecked' on ChEMBL). This is to avoid the overlap of very similar tasks during training and inference.

● Test tasks must have over 96 datapoints, to enable model comparison for a range of support set sizes.

● Test tasks must have a ratio of active compounds between 0.3 and 0.7, to avoid strongly imbalanced data affecting the model comparison. Some methods might be better because they overcome the data imbalance problem, not the low data problem which is what we focus on.

Dataset statistics. FSL-CP contains 201 modelling tasks for 10 526 unique compounds, with only 2.58% of the label matrix filled. The number of compounds for each task and their active ratio are visualised in (Fig. 2A) and (Fig. 2B), respectively. It is worth noting that the majority of the compounds have 4 replicates, as per the design of the cell painting assay. However, there are cases where there are fewer or more replicates
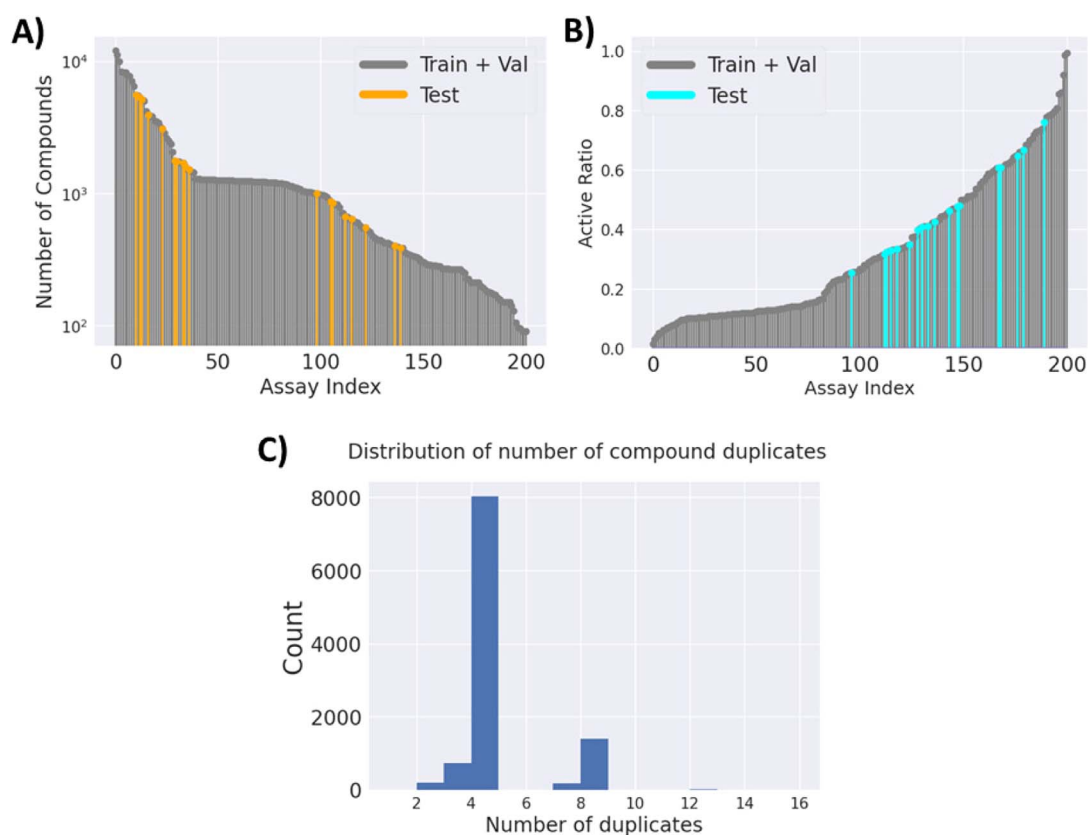
Fig. 2 FSL-CP data statistics. (A) Number of compounds for every modelling task. (B) Ratio of active compounds for every modelling task. Test tasks (in turquoise) have an active ratio between 0.3 and 0.7. (C) Distribution of compound duplicates. Most have 4 duplicates as per experimental design, but there can be more or less duplicates, due to omission of low-quality images, or repeated purchases of compounds.

(Fig. 2C), potentially due to the omission of low-quality images and repeated purchases of some compounds.

2.2 Evaluation

Few-shot prediction. In order to simulate a low-data setting when evaluating models, we sample from each task in a stratified manner a small number M of datapoints for the support set and 32 datapoints for the query set. The models are then trained on a binary classification task on the support set and evaluated on the query set. In the literature, this sampled subset is called a M-samples 2-shot episode, where 'samples' refer to available data (size of the support set) and 'shot' refers to the number of classes to predict, which is two for binary classification.

For every test task, we report model performances averaged over 100 episodes in order to eliminate variations from sampling. Additionally, the results are recorded over a range of support set sizes M: 8, 16, 32, 64, 96, to monitor how well models perform as the size of available data increases.

Metrics. We mainly report and discuss results using area under the receiver operating characteristic curve (AUROC). AUROC comes with many benefits, such as ranking predictions without a decision threshold, meaning predictions can be compared without needing to be rounded to 0 or 1. At the same time, the active ratios of tasks in D_{test} are not so imbalanced that they make AUROC misleading.

In addition, the results reported in terms of F1 score, balanced accuracy, Cohen's kappa, and ΔAUPRC[22] can also be found in the ESI.†

2.3 Benchmark models

In this section, we provide a detailed description of different modelling paradigms for this particular few-shot problem. The code for all of the models and the training/inference scripts can be found at **https://github.com/czodrowskilab/FSL_CP**. As a naming convention, models with _img are trained directly on the images, _cp means that they are trained on the original CP features, and _cp+ means that they are trained on the enhanced CP features.

Single-task models. Traditionally, modelling of tasks in drug discovery is solely a single-task, with models such as random forest or gradient boosting algorithms on top of fingerprints or curated phys-chem properties.[31–34] In these settings, auxiliary tasks are not used. Here, we mimic the same procedure by assessing the performance of logistic regression (LR), XGBoost, and a single-task fully connected neural network (FNN), on both the original and enhanced CP features. For each prediction task of each model we run a randomised hyperparameter grid search using the library scikit-learn,[35] considering 10 hyperparameter configurations per run. We report the results of the two best performing single-task models: LR on enhanced CP features (logistic_cp+) and FNN on original CP features (singletask_cp).

Multi-task models. Multi-task models have been a staple in the drug discovery field, being adopted by many academic and industry groups for various prediction tasks.[16,36,37] These models consist of multiple 'heads', each specialised on one task, on top of a shared 'trunk'. The trunk aims to learn a common representation across tasks, which allows it to learn knowledge transferable between tasks and improve performance of each one.

For our benchmark, the same FNN model as that in the single-task case is used, but with a head of length 183 instead. Pretraining and validation are performed using 183 auxiliary tasks in D_{train} and D_{val} in a multi-task manner. Then the weights are frozen, and the head is replaced with a new one of length 1 for fine-tuning. During evaluation, for each episode, the same frozen model has its last layer fine-tuned using the support set, evaluated on the query set, and reverted back to the state before fine-tuning. We tried training on both sets of CP features but neither led to drastic improvements over the other. We decided to report the result for the model trained on the original CP to reflect the methods by Simm *et al.* This model is denoted as multitask_cp.

Meta-learning models. Inspired by human's ability to learn certain tasks very quickly with prior knowledge, meta-learning methods aim to tackle the problem of adapting to new tasks efficiently with only a few training examples. The idea is still the same: pretraining to gain transferable knowledge to generalise to new tasks. But the meta-learning methods introduce the idea of training in the same way as testing.[38] In particular, if we evaluate the model on M-sample 2-shot episodes, then we can mimic that setting during pretraining to encourage fast adaptation. That means that during pretraining, we sample an episode from D_{train} the same way we sample from D_{test} and accumulate the loss from many episodes to update our models' weights. This process is called episodic training.

One subclass of meta-learning is a metric-based method, which tries to learn a distance function over data samples. For example, the prototypical network[17] uses a backbone model to generate an embedding. Then classification is made using k-means clustering based on the Euclidean distance from the embedding to the cluster prototypes. Since the backbone for a prototypical network can be any kind of embedding generator, we try 2 versions: a ResNet50 and an FNN backbone, which generate embeddings from CP images and CP features, respectively. These models are named protonet_img, protonet_cp and protonet_cp+.

The optimisation-based method is another subclass of meta-learning. This approach intends to make gradient-based optimisation converge within a small number of optimisation steps. MAML[18] (model-agnostic meta-learning) achieves this by obtaining good weight initialisation through pretraining, so that fine-tuning to unseen tasks can be more efficient. Thanks to MAML working with any algorithm that uses gradient descent, we provide the results of ResNet50 and an FNN after being trained by MAML (denoted as maml_img and maml_cp+).

It is important to mention that, unlike feature-based models, image-based models are highly computationally expensive to train. Hence to train these models and tune the hyperparameters in a reasonable time frame, only one out of six available views is used, plus random cropping and down-sizing of images are performed. With an 11GiB NVIDIA GeForce RTX

2080 Ti, the training and inference for one hyperparameter configuration take between 1 and 2 weeks, depending on the model.

3 Results

In order to compare performances of different methods benchmarked on FSL-CP, we plot the mean AUROC across 18 test tasks of each method at different support set sizes (Fig. 3A). In addition, a paired Wilcoxon sign-rank test is performed for each pair of models as demonstrated in Table 1, with the alternative hypothesis that the method in the left column outperforms the method in the upper row. These figures also provide insight into how the performance of each model changes as the amount of available data increases.

Fig. 3A indicates that the best performing models overall are variants of prototypical networks protonet_cp+ and protonet_cp, followed closely by multitask_cp, although according to the Wilcoxon signed-rank test, protonet_cp+ only outperforms multitask_cp for medium-sized datasets (support set size 32). There is no sufficient evidence to reject the null hypothesis that they perform equally well at other support set sizes with $\alpha = 0.01$. We note that multitask_cp even slightly outperforms protonet_cp+ and protonet_cp at support set size 8.

The best single-task model singletask_cp is surprisingly powerful, being able to catch up with maml_cp+ at lower support set size, and outperforms it by a wide margin at large support set size. For these single-task models with no pretraining, the availability of more data in the support set can lead to dramatic improvements in performance. It is highly likely that their performances will keep improving and eventually might overtake other methods beyond support set size 96. In contrast, improvements in AUROC scores of meta-learning methods slow down at higher support set size and even drop as in the case of maml_cp+. However, it is worth noting that at support set size 96, some test tasks are excluded from the evaluation process due to insufficient data points. Plus, fewer tasks in D_{train} and D_{val} are included in the pretraining for meta-learning models at high support set size, due to the fact that there may not be enough datapoints to sample for episodic training. All of these factors can affect meta-learning methods' performance in higher data setting.

Image-based models such as protonet_img and maml_img substantially under-perform compared to other feature-based methods, likely because only one view out of six is used and down-sizing of images of fairly small cells leads to drastic information loss.

We also try to leverage deep-learning-based features by concatenating the original CP features with a ResNet50
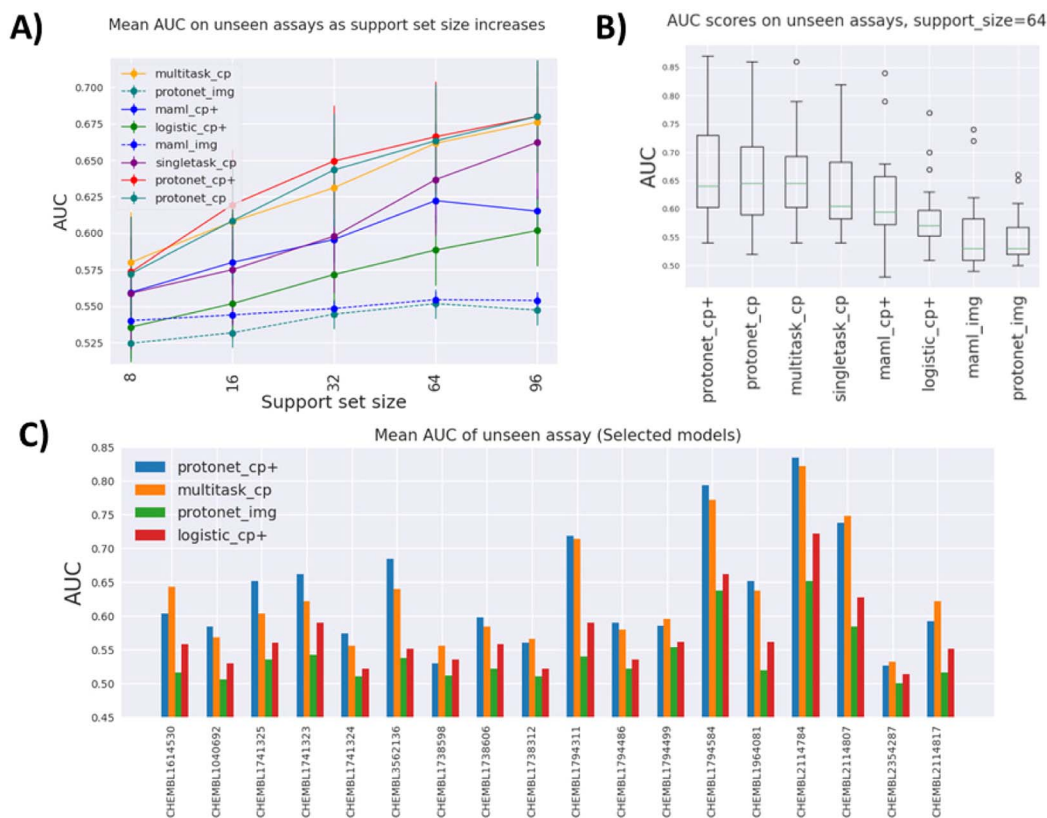
Fig. 3 Comparison of different models benchmarked on FSL-CP. (A) Mean AUROC on test tasks as support set size increases. As there are more data available, other methods start to catch up to meta-learning models. (B) Distribution of AUROC across all test tasks at support set size 64. The best models tend to have larger AUROC variance. (C) Mean AUROC of selected models for each task across all support set sizes. For most tasks, pretraining on auxiliary tasks leads to an improvement over single-task models. However, for a few tasks this is not the case.

Table 1 p-values of the one-sided paired Wilcoxon sign-rank test[a] with an alternative hypothesis being that the method in the left column outperforms the method in the upper row. Entries left blank indicate a p-value greater or equal to 9.99×10^{-1}

	Protonet_cp	Multitask_cp	Singletask_cp	Maml_cp+	Logistic_cp+	Maml_img	Protonet_img
(a) Support set size 8							
Protonet_cp+	3.60×10^{-1}	7.89×10^{-1}	1.56×10^{-1}	3.79×10^{-1}	$\mathbf{1.05 \times 10^{-3}}$	$\mathbf{3.09 \times 10^{-3}}$	$\mathbf{5.38 \times 10^{-4}}$
Protonet_cp		8.90×10^{-1}	2.74×10^{-1}	6.12×10^{-1}	$\mathbf{1.79 \times 10^{-3}}$	$\mathbf{5.23 \times 10^{-3}}$	$\mathbf{4.52 \times 10^{-4}}$
Multitask_cp			$\mathbf{3.96 \times 10^{-2}}$	3.04×10^{-1}	$\mathbf{2.69 \times 10^{-4}}$	$\mathbf{1.11 \times 10^{-3}}$	$\mathbf{1.43 \times 10^{-4}}$
Singletask_cp				6.03×10^{-1}	$\mathbf{3.09 \times 10^{-3}}$	8.05×10^{-2}	$\mathbf{1.21 \times 10^{-3}}$
Maml_cp+					8.84×10^{-2}	$\mathbf{1.92 \times 10^{-2}}$	$\mathbf{2.74 \times 10^{-2}}$
Logistic_cp+						6.42×10^{-1}	$\mathbf{9.16 \times 10^{-3}}$
Maml_img							$\mathbf{3.47 \times 10^{-2}}$
(b) Support set size 16							
Protonet_cp+	$\mathbf{1.45 \times 10^{-2}}$	5.42×10^{-2}	$\mathbf{9.36 \times 10^{-4}}$	$\mathbf{2.77 \times 10^{-3}}$	$\mathbf{2.49 \times 10^{-4}}$	$\mathbf{5.34 \times 10^{-5}}$	$\mathbf{7.63 \times 10^{-6}}$
Protonet_cp		5.41×10^{-1}	$\mathbf{1.08 \times 10^{-2}}$	$\mathbf{2.21 \times 10^{-2}}$	$\mathbf{8.53 \times 10^{-4}}$	$\mathbf{5.35 \times 10^{-4}}$	$\mathbf{2.63 \times 10^{-4}}$
Multitask_cp			$\mathbf{5.22 \times 10^{-4}}$	$\mathbf{1.13 \times 10^{-2}}$	$\mathbf{2.08 \times 10^{-4}}$	$\mathbf{9.54 \times 10^{-5}}$	$\mathbf{1.46 \times 10^{-4}}$
Singletask_cp				6.51×10^{-1}	$\mathbf{1.68 \times 10^{-3}}$	$\mathbf{3.49 \times 10^{-2}}$	$\mathbf{3.43 \times 10^{-4}}$
Maml_cp+					$\mathbf{2.01 \times 10^{-2}}$	$\mathbf{2.98 \times 10^{-3}}$	$\mathbf{1.03 \times 10^{-3}}$
Logistic_cp+						2.48×10^{-1}	$\mathbf{1.50 \times 10^{-3}}$
Maml_img							1.27×10^{-1}
(c) Support set size 32							
Protonet_cp+	8.63×10^{-2}	$\mathbf{7.97 \times 10^{-3}}$	$\mathbf{3.83 \times 10^{-4}}$	$\mathbf{1.42 \times 10^{-4}}$	$\mathbf{1.46 \times 10^{-4}}$	$\mathbf{3.81 \times 10^{-6}}$	$\mathbf{3.81 \times 10^{-6}}$
Protonet_cp		6.49×10^{-2}	$\mathbf{1.46 \times 10^{-3}}$	$\mathbf{2.67 \times 10^{-4}}$	$\mathbf{2.67 \times 10^{-5}}$	$\mathbf{1.74 \times 10^{-4}}$	$\mathbf{1.14 \times 10^{-5}}$
Multitask_cp			$\mathbf{4.03 \times 10^{-4}}$	$\mathbf{4.56 \times 10^{-3}}$	$\mathbf{3.81 \times 10^{-6}}$	$\mathbf{3.81 \times 10^{-6}}$	$\mathbf{3.81 \times 10^{-6}}$
Singletask_cp				3.61×10^{-1}	$\mathbf{2.80 \times 10^{-3}}$	$\mathbf{1.22 \times 10^{-3}}$	$\mathbf{2.56 \times 10^{-4}}$
Maml_cp+					$\mathbf{3.69 \times 10^{-2}}$	$\mathbf{1.65 \times 10^{-3}}$	$\mathbf{5.23 \times 10^{-4}}$
Logistic_cp+						$\mathbf{7.97 \times 10^{-3}}$	$\mathbf{1.36 \times 10^{-4}}$
Maml_img							2.55×10^{-1}
(d) Support set size 64							
Protonet_cp+	2.62×10^{-1}	3.43×10^{-1}	$\mathbf{6.97 \times 10^{-3}}$	$\mathbf{4.40 \times 10^{-4}}$	$\mathbf{7.63 \times 10^{-6}}$	$\mathbf{3.81 \times 10^{-6}}$	$\mathbf{3.81 \times 10^{-6}}$
Protonet_cp		3.88×10^{-1}	$\mathbf{1.46 \times 10^{-2}}$	$\mathbf{6.05 \times 10^{-4}}$	$\mathbf{1.91 \times 10^{-5}}$	$\mathbf{1.46 \times 10^{-4}}$	$\mathbf{7.63 \times 10^{-6}}$
Multitask_cp			$\mathbf{2.07 \times 10^{-4}}$	$\mathbf{2.47 \times 10^{-4}}$	$\mathbf{3.81 \times 10^{-6}}$	$\mathbf{3.81 \times 10^{-6}}$	$\mathbf{3.81 \times 10^{-6}}$
Singletask_cp				9.31×10^{-2}	$\mathbf{1.43 \times 10^{-4}}$	$\mathbf{3.81 \times 10^{-6}}$	$\mathbf{3.81 \times 10^{-6}}$
Maml_cp+					$\mathbf{4.10 \times 10^{-3}}$	$\mathbf{1.14 \times 10^{-5}}$	$\mathbf{1.14 \times 10^{-5}}$
Logistic_cp+						$\mathbf{2.02 \times 10^{-3}}$	$\mathbf{2.11 \times 10^{-4}}$
Maml_img							4.18×10^{-1}
(e) Support set size 96							
Protonet_cp+	6.14×10^{-1}	2.84×10^{-1}	7.73×10^{-2}	$\mathbf{7.25 \times 10^{-5}}$	$\mathbf{3.81 \times 10^{-6}}$	$\mathbf{3.81 \times 10^{-6}}$	$\mathbf{3.81 \times 10^{-6}}$
Protonet_cp		2.09×10^{-1}	6.44×10^{-2}	$\mathbf{2.29 \times 10^{-4}}$	$\mathbf{2.16 \times 10^{-4}}$	$\mathbf{3.81 \times 10^{-6}}$	$\mathbf{3.81 \times 10^{-6}}$
Multitask_cp			$\mathbf{4.00 \times 10^{-2}}$	$\mathbf{1.45 \times 10^{-4}}$	$\mathbf{3.81 \times 10^{-6}}$	$\mathbf{3.81 \times 10^{-6}}$	$\mathbf{3.81 \times 10^{-6}}$
Singletask_cp				$\mathbf{3.36 \times 10^{-4}}$	$\mathbf{1.44 \times 10^{-4}}$	$\mathbf{3.81 \times 10^{-6}}$	$\mathbf{3.81 \times 10^{-6}}$
Maml_cp+					1.85×10^{-1}	$\mathbf{1.14 \times 10^{-5}}$	$\mathbf{4.44 \times 10^{-4}}$
Logistic_cp+						$\mathbf{3.21 \times 10^{-4}}$	$\mathbf{3.81 \times 10^{-6}}$
Maml_img							2.33×10^{-1}

[a] The test compares mean AUROC (over 100 episodes) of models in 18 test tasks. Marked in bold are significant p-values at $\alpha = 0.01$.

embedding of size 1000. While in some cases it leads to higher AUROC, as evidenced by the fact that many models use the enhanced feature, the improvements are somewhat minute. For example, when comparing protonet_cp+ against protonet_cp, Table 1 shows insufficient evidence of improvement across tasks, and as shown in Fig. 3A, the additional features lead to only small improvements at support set sizes 16, 32 and 64. However, this still poses an interesting question for future research: how meaningful embedding from cell images can be produced using deep learning methods.

Better performing models have a larger spread of AUROC across test tasks, as shown in Fig. 3B, indicating that model performances are fairly dependent on tasks. This is further demonstrated in Fig. 3C, where some tasks (e.g. CHEMBL2114784) consistently show high AUROC across models and some (e.g. CHEMBL2354287) are not predictive at all. Additionally, for some tasks protonet_cp+ is the best method, but in a few other cases multitask_cp or singletask_cp is the better method.

Fig. 3C also gives insight on how much pretraining on auxiliary tasks benefits prediction. Again, this is highly task-dependent. Some tasks benefit greatly from pretraining (CHEMBL3562136 and CHEMBL2114807), as seen from the improvements of the two pretraining models over the single-task models. However, pretraining can offer no improvement, or even be detrimental in tasks such as CHEMBL1738598 and CHEMBL1738312.

4 Discussion

We have presented FSL-CP, a dataset for small molecule activity few-shot prediction using cell microscopy images. This few-shot challenge mimics a screening process in early stage drug discovery, where the aim is to identify potent compounds targeting a specific protein from high-content cell images with little data. Previous efforts have been made to benchmark few-shot methods on molecules as graph-structured data.[22] But in machine learning, the primary focus of few-shot learning has been in the computer vision and natural language processing domains. The fact that our dataset uses cell images as a molecular representation opens up opportunities to adapt state-of-the-art ideas from computer vision to enhance modeling.

This dataset allows us to establish benchmarks that compare the performances of different few-shot learning paradigms. Our result indicates that the feature-based prototypical network and multitask FNN pretrained on auxiliary tasks generally perform well across all support set sizes. We also observe improvement in performance slowing down for meta-learning methods at high support set size, in contrast to single-task methods, which greatly benefit from the availability of more available data. However, more labelled compounds and their cell painting data are needed in order to accurately point out whether eventually single-task models outperform pretrained models, and if yes, at what support set size.

Image-based models underperform on our benchmark, and the fact that each datapoint consists of six high-definition five-channel images makes it tremendously computationally expensive to train. We had to use only one randomly cropped, downsized image to train the models in a reasonable time-frame with our infrastructure, and this leads to high information loss. Training on full-resolution cell images has been shown to offer better performance than that on CP features in some settings.[25] However, in realistic drug discovery projects, larger-size images are used, and there are typically more compounds and more prediction tasks. These make pretraining on full-resolution images difficult, especially if the model needs to be regularly retrained.

A less expensive way to leverage the power of computer vision is to enhance the CP feature with the embedding of an image using a pretrained model such as ResNet or Inception. We tried a simple approach with ResNet50 as an embedding generator, which yielded small improvements. Since most vision models are pretrained on ImageNet, this suggests that there is some transferable knowledge obtained from training on a large unrelated image database, but not enough to make a significant improvement. We expect that a more informative embedding can be achieved by pretraining the embedding generator end-to-end on cell images with a more relevant pretraining task, such as multi-task or contrastive learning.[39,40]

The benchmark also provides insight on how effective transferring knowledge from pretraining models on auxiliary tasks is to new tasks. Mostly, new tasks benefit from such a pretraining scheme, but the degree to which different tasks improve varies. To what degree a new task benefits from pretraining is still an open question for research. As a general observation, it seems that already predicted tasks tend to benefit more from pretraining. Companies aiming to pretrain their models on auxiliary tasks can use a combination of tasks from public sources as well as their own databases to benefit from as much data as possible.

FSL-CP offers a promising and interesting research question, though not one without unique challenges of its own. Through this study, we hope to encourage further research in few-shot and computer vision methods in the domain of cell imaging. The code for generating the dataset, model training, inference, and tutorials is publicly available on GitHub.

Data availability

The dataset, model codes, plots and results are all publicly available on Github: **https://github.com/czodrowskilab/FSL_CP**. In addition, since the FSL-CP dataset is curated from two larger public databases: ChEMBL and Broad Institute, the code for data processing and curation is also available on Github **https://github.com/czodrowskilab/FSL_CP_DataPrep**.

Author contributions

S. V. H. and P. C. formulated the project. S. V. H. curated the data. L. L. coded and trained the single-task models. S. V. H. coded and trained the multi-task and the meta-learning models. S. V. H. wrote the manuscript, and all authors contributed to revising the manuscript.

Conflicts of interest

There are no conflicts to declare.

Acknowledgements

Notes and references

1 J. G. Moffat, J. Rudolph and D. Bailey, *Nat. Rev. Drug Discovery*, 2014, **13**, 588–602.
2 C. M. Johannessen, P. A. Clemons and B. K. Wagner, *Trends Genet.*, 2015, **31**, 16–23.

3 D. Herman, M. M. Kańduła, L. G. A. Freitas, C. van Dongen, T. Le Van, N. Mesens, S. Jaensch, E. Gustin, L. Micholt, C.-H. Lardeau, C. Varsakelis, J. Reumers, S. Zoffmann, Y. Will, P. J. Peeters and H. Ceulemans, *Chem. Res. Toxicol.*, 2023, **36**, 1028–1036.

4 M.-A. Bray, S. M. Gustafsdottir, M. H. Rohban, S. Singh, V. Ljosa, K. L. Sokolnicki, J. A. Bittker, N. E. Bodycombe, V. Dančík, T. P. Hasaka, C. S. Hon, M. M. Kemp, K. Li, D. Walpita, M. J. Wawer, T. R. Golub, S. L. Schreiber, P. A. Clemons, A. F. Shamji and A. E. Carpenter, *GigaScience*, 2017, **6**, 1–5.

5 J. C. Caicedo, S. Singh and A. E. Carpenter, *Curr. Opin. Biotechnol.*, 2016, **39**, 134–142.

6 F. Reisen, A. Sauty de Chalon, M. Pfeifer, X. Zhang, D. Gabriel and P. Selzer, *Assay Drug Dev. Technol.*, 2015, **13**, 415–427.

7 D. W. Young, A. Bender, J. Hoyt, E. McWhinnie, G.-W. Chirn, C. Y. Tao, J. A. Tallarico, M. Labow, J. L. Jenkins, T. J. Mitchison and Y. Feng, *Nat. Chem. Biol.*, 2008, **4**, 59–68.

8 V. Ljosa, P. D. Caie, R. Ter Horst, K. L. Sokolnicki, E. L. Jenkins, S. Daya, M. E. Roberts, T. R. Jones, S. Singh, A. Genovesio, P. A. Clemons, N. O. Carragher and A. E. Carpenter, *J. Biomol. Screening*, 2013, **18**, 1321–1329.

9 C. Collinet, M. Stöter, C. R. Bradshaw, N. Samusik, J. C. Rink, D. Kenski, B. Habermann, F. Buchholz, R. Henschel, M. S. Mueller, W. E. Nagel, E. Fava, Y. Kalaidzidis and M. Zerial, *Nature*, 2010, **464**, 243–249.

10 F. Fuchs, G. Pau, D. Kranz, O. Sklyar, C. Budjan, S. Steinbrink, T. Horn, A. Pedal, W. Huber and M. Boutros, *Mol. Syst. Biol.*, 2010, **6**, 370.

11 M. Garcia de Lomana, P. A. Marin Zapata and F. Montanari, *Chem. Res. Toxicol.*, 2023, **36**, 1107–1120.

12 A. Liu, S. Seal, H. Yang and A. Bender, *SLAS Discovery*, 2023, **28**, 53–64.

13 M. Akbarzadeh, I. Deipenwisch, B. Schoelermann, A. Pahl, S. Sievers, S. Ziegler and H. Waldmann, *Cell Chem. Biol.*, 2022, **29**, 1053–1064.

14 S. Seal, H. Yang, M.-A. Trapotsi, S. Singh, J. Carreras-Puigvert, O. Spjuth and A. Bender, *J. Cheminf.*, 2023, **15**, 56.

15 S. Seal, J. Carreras-Puigvert, M.-A. Trapotsi, H. Yang, O. Spjuth and A. Bender, *Commun. Biol.*, 2022, **5**, 858.

16 J. Simm, G. Klambauer, A. Arany, M. Steijaert, J. K. Wegner, E. Gustin, V. Chupakhin, Y. T. Chong, J. Vialard, P. Buijnsters, I. Velter, A. Vapirev, S. Singh, A. E. Carpenter, R. Wuyts, S. Hochreiter, Y. Moreau and H. Ceulemans, *Cell Chem. Biol.*, 2018, **25**, 611–618.

17 J. Snell, K. Swersky and R. S. Zemel, *arXiv*, 2017, arXiv:1703.05175 [cs.LG], DOI: **10.48550/arXiv.1703.05175**.

18 C. Finn, P. Abbeel and S. Levine, *arXiv*, 2017, arXiv:1703.03400 [cs.LG], DOI: **10.48550/arXiv.1703.03400**.

19 T. B. Brown, B. Mann, N. Ryder, M. Subbiah, J. Kaplan, P. Dhariwal, A. Neelakantan, P. Shyam, G. Sastry, A. Askell, S. Agarwal, A. Herbert-Voss, G. Krueger, T. Henighan, R. Child, A. Ramesh, D. M. Ziegler, J. Wu, C. Winter, C. Hesse, M. Chen, E. Sigler, M. Litwin, S. Gray, B. Chess, J. Clark, C. Berner, S. McCandlish, A. Radford, I. Sutskever and D. Amodei, *arXiv*, 2020, arXiv:2005.14165 [cs.CL], DOI: **10.48550/arXiv.2005.14165**.

20 R. Geng, B. Li, Y. Li, X. Zhu, P. Jian and J. Sun, *arXiv*, 2019, arXiv:1902.10482 [cs.CL], DOI: **10.48550/arXiv.1902.10482**.

21 O. Vinyals, C. Blundell, T. Lillicrap, K. Kavukcuoglu and D. Wierstra, *arXiv*, 2017, arXiv:1606.04080 [cs.LG], DOI: **10.48550/arXiv.1606.04080**.

22 M. Stanley, J. F. Bronskill, K. Maziarz, H. Misztela, J. Lanini, M. Segler, N. Schneider and M. Brockschmidt, *NeurIPS 2021 Track Datasets and Benchmarks*, 2021.

23 D. Mendez, A. Gaulton, A. P. Bento, J. Chambers, M. De Veij, E. Félix, M. Magariños, J. Mosquera, P. Mutowo, M. Nowotka, M. Gordillo-Marañón, F. Hunter, L. Junco, G. Mugumbate, M. Rodriguez-Lopez, F. Atkinson, N. Bosc, C. Radoux, A. Segura-Cabrera, A. Hersey and A. Leach, *Nucleic Acids Res.*, 2018, **47**, D930–D940.

24 A. Carpenter, T. Jones, M. Lamprecht, C. Clarke, I. Kang, O. Friman, D. Guertin, J. Chang, R. Lindquist, J. Moffat, P. Golland and D. Sabatini, *Genome Biol.*, 2006, **7**, R100.

25 M. Hofmarcher, E. Rumetshofer, D.-A. Clevert, S. Hochreiter and G. Klambauer, *J. Chem. Inf. Model.*, 2019, **59**, 1163–1171.

26 K. He, X. Zhang, S. Ren and J. Sun, *arXiv*, 2015, arXiv:1512.03385 [cs.CV], DOI: **10.48550/arXiv.1512.03385**.

27 O. Russakovsky, J. Deng, H. Su, J. Krause, S. Satheesh, S. Ma, Z. Huang, A. Karpathy, A. Khosla, M. Bernstein, A. C. Berg and L. Fei-Fei, *Int. J. Comput. Vis.*, 2015, **115**, 211–252.

28 L. Schiff, B. Migliori, Y. Chen, D. Carter, C. Bonilla, J. Hall, M. Fan, E. Tam, S. Ahadi, B. Fischbacher, A. Geraschenko, C. J. Hunter, S. Venugopalan, S. DesMarteau, A. Narayanaswamy, S. Jacob, Z. Armstrong, P. Ferrarotto, B. Williams, G. Buckley-Herd, J. Hazard, J. Goldberg, M. Coram, R. Otto, E. A. Baltz, L. Andres-Martin, O. Pritchard, A. Duren-Lubanski, A. Daigavane, K. Reggio, P. C. Nelson, M. Frumkin, S. L. Solomon, L. Bauer, R. S. Aiyar, E. Schwarzbach, S. A. Noggle, F. J. Monsma, D. Paull, M. Berndl, S. J. Yang, B. Johannesson and N. G. S. C. A. Team, *Nat. Commun.*, 2022, **13**, 1590.

29 C. Szegedy, W. Liu, Y. Jia, P. Sermanet, S. Reed, D. Anguelov, D. Erhan, V. Vanhoucke and A. Rabinovich, *arXiv*, 2014, arXiv:1409.4842 [cs.CV], DOI: **10.48550/arXiv.1409.4842**.

30 C. Szegedy, V. Vanhoucke, S. Ioffe, J. Shlens and Z. Wojna, *arXiv*, 2015, arXiv:1512.00567 [cs.CV], DOI: **10.48550/arXiv.1512.00567**.

31 D. Rogers and M. Hahn, *J. Chem. Inf. Model.*, 2010, **50**, 742–754.

32 A. Mauri, V. Consonni, M. Pavan and R. Todeschini, *MATCH Communications in Mathematical and in Computer Chemistry*, 2006, **56**, 237–248.

33 O. Soufan, W. Ba-alawi, A. Magana-Mora, M. Essack and V. B. Bajic, *Sci. Rep.*, 2018, **8**, 9110.

34 D. Butina, M. D. Segall and K. Frankcombe, *Drug Discovery Today*, 2002, **7**, S83–S88.

35 F. Pedregosa, G. Varoquaux, A. Gramfort, V. Michel, B. Thirion, O. Grisel, M. Blondel, P. Prettenhofer, R. Weiss, V. Dubourg, J. Vanderplas, A. Passos, D. Cournapeau, M. Brucher, M. Perrot and E. Duchesnay, *J. Mach. Learn. Res.*, 2011, **12**, 2825–2830.

36 A. Mayr, G. Klambauer, T. Unterthiner and S. Hochreiter, *Front. Environ. Res.*, 2016, **3**, 80.

37 W. Hu, B. Liu, J. Gomes, M. Zitnik, P. Liang, V. Pande and J. Leskovec, *arXiv*, 2020, arXiv:1905.12265 [cs.LG], DOI: **10.48550/arXiv.1905.12265**.

38 L. Weng, **https://www.lilianweng.github.io**, 2018.

39 K. Chaitanya, E. Erdil, N. Karani and E. Konukoglu, *arXiv*, 2020, arXiv:2006.10511 [cs.CV], DOI: **10.48550/arXiv.2006.10511**.

40 A Radford, J. W. Kim, C. Hallacy, A. Ramesh, G. Goh, S. Agarwal, G. Sastry, A. Askell, P. Mishkin, J. Clark, G. Krueger and I. Sutskever, *arXiv*, 2021, arXiv:2103.00020 [cs.CV], DOI: **10.48550/arXiv.2103.00020**.